Research Square

Preprints are preliminary reports that have not undergone peer review.
They should not be considered conclusive, used to inform clinical practice,
or referenced by the media as validated information.

Optimal Sail Angles to Drive Circular Motion

Rory Ward

rory.ward@student.unimelb.edu.au

The University of Melbourne

Ian Hewitt

University of Oxford

Graham Benham

University College London

Research Article

Keywords: Sail aerodynamics, Circular motion, Optimisation, Wind energy

Posted Date: November 2nd, 2026

DOI: https://doi.org/10.21203/rs.3.rs-11373823/v1

License: This work is licensed under a Creative Commons Attribution 4.0 International License.
Read Full License

Additional Declarations: Competing interest reported. Rory Ward received payment from VerdErg Renewable Energy Ltd for work undertaken as part of an industry project during their Master's degree, on which this study is based. The other authors declare that they have no known competing financial interests or personal relationships that could have appeared to influence the work reported in this paper.

Optimal Sail Angles to Drive Circular Motion

Rory Ward[1*], Ian Hewitt[2] and Graham Benham[3]

[1*]School of Mathematics and Statistics, The University of Melbourne, Parkville, 3010, VIC, Australia.
[2]Mathematical Institute, University of Oxford, Oxford, OX2 6GG, UK.
[3]Department of Mechanical Engineering, University College London, Gower Street, London, WC1E 6BT, UK.

*Corresponding author(s). E-mail(s): rory.ward@student.unimelb.edu.au;
Contributing authors: ian.hewitt@maths.ox.ac.uk; g.benham@ucl.ac.uk;

Abstract

This study examines the optimisation of sail or airfoil angles to generate torque in circular motion, focussing on the interplay of lift and drag forces under constant wind conditions. Motivated by potential application to wind energy production and storage, the model considers a sail mounted on the surface of a rotating flywheel and identifies optimal sail orientations to maximise torque, highlighting dependence on the ratio of sail speed to wind speed. That is, when the sail travels slower than the wind speed, there are positions where the sail can utilise drag whilst travelling downwind; at higher speeds, this is not possible, and maximising lift whilst mitigating drag is crucial.

We extend the model to a system with multiple evenly spaced sails, showing that increasing the sail count reduces torque variance, ensuring more stable energy production. Additionally, the analysis identifies a critical speed threshold above which the sails hinder rotation, acting only to decelerate the flywheel. Furthermore, sail placement can influence system performance, where the sail radius affects the torque generated and the optimal radius depends upon the rotational speed. These findings underscore the importance of precise control over sail parameters to enhance energy capture efficiency.

Keywords: Sail aerodynamics, Circular motion, Optimisation, Wind energy

1 Introduction

As society moves towards cleaner energy systems, significant challenges arise concerning the reliability of renewable energy generation. One of the primary difficulties is the variability in the output from weather-dependent technologies, such as wind, solar, and tidal energy generation [1]. Addressing this variability requires the use of energy storage systems that store surplus energy during periods of low demand and release it when demand exceeds supply. For example, to achieve the national goal of net-zero carbon emissions by 2050 [2], it is projected that the UK will need energy storage systems available to provide 29 GW of power to the national grid by 2030, and up to 51 GW by 2050. However, there is currently only capacity to provide 5 GW, and therefore supply and demand must be matched closely to reach such targets [3]. As such, the development of more cost-effective and sustainable energy storage technologies is vital [4].

One energy storage system being employed in large scales is pumped hydropower, which pumps water to a higher elevation when there is excess energy, and harnesses the gravitational potential energy available when in deficit. The largest single energy storage facility in the UK is the Dinorwig Power Station, which has capacity to supply 1.7 GW for up to 5 hours [5]. Despite the advantages of high output and storage capacity, pumped hydropower systems are expensive and geographically-constrained. Another common energy storage facility, for both national grid storage as well as on much smaller scales, is electrochemical batteries. These are relatively inexpensive due to their high energy densities [6], but come with their own challenges including degradation over time [7], fire risks [6, 8], and adverse effects on the environment [4, 9]. Many other systems are also currently being used in smaller scales, such as thermal energy storage [10, 11], hydrogen electrolysis [12], and compressed air storage [13]. Whilst continuous improvement of existing technologies remains essential, innovative approaches to energy storage should also be pursued to meet future demands.

One such possibility is a patented device termed a *Gyrerg* [14], being developed by renewable energy company VerdErg Renewable Energy Limited [15]. It takes the form of a concrete flywheel that floats on the surface of a body of water, and stores energy mechanically by rotating. In order to store significant quantities of energy, *Gyrerg* would have to be very large, potentially with a radius on the order of 1 km, and would be partially supported by a pressurised air cushion beneath, reducing the wetted surface area. A potential method to offset the losses due to hydrodynamic drag is to place a number of sails on the surface of the flywheel. These sails would be constrained to travel in circular motion and could potentially generate additional torque. A conceptual design of *Gyrerg* with sails on top is shown in Figure 1, which shows the potential scale of such a device.

Inspired by this industrial application, this paper presents a simplified two-dimensional mathematical model regarding the potential torque generated from sails atop the surface of a flywheel, with the aim of determining the optimal orientation angle for a sail as it travels in circular motion. Unlike stationary sails, these could rotate at high speeds, continuously adjusting their orientation in response to the wind, thus creating a dynamic and complex environment for sail control. This scenario introduces



Fig. 1: A conceptual design of *Gyrerg* with sails on top. Taken with permission from [14].

the challenge of maintaining optimal alignment with constantly varying apparent wind experienced in circular motion.

The dynamics of sail forces have been extensively studied in both steady-state and dynamic sailing contexts. Previous research has highlighted the aerodynamic forces acting on sails, including the lift and drag components, and their dependence on the sail's angle of attack and the relative wind speed [16–19]. The effect of dynamic sailing conditions has also been considered for varying wind and sea conditions [20–22].

A similar concept to the present problem is that of vertical-axis wind turbines (VAWTs), as both involve surfaces moving in circular motion through an ambient flow with the goal of producing torque. In particular, Darrieus turbines and cycloturbines experience continuously changing apparent wind conditions as the blades rotate, causing the angle of attack and aerodynamic forces to vary throughout the rotation cycle [23]. As a result, considerable research has been devoted to understanding how blade orientation affects the performance of these devices.

Traditional Darrieus turbines employ fixed-pitch blades, meaning that the blade orientation is fixed relative to the rotor, and the angle of attack varies solely due to the blade position around the rotation. Whilst mechanically simpler, fixed-pitch turbines can suffer from poor starting characteristics and large variations in aerodynamic loading. To overcome these limitations, variable-pitch configurations have been developed in which the blade orientation changes throughout the rotation cycle. These systems, often referred to as cycloturbines, have been shown to improve both starting torque and aerodynamic efficiency compared with fixed-pitch designs [24].

The optimisation of blade pitch angles in vertical-axis wind turbines has been widely studied using both numerical and experimental methods. For fixed-pitch configurations, optimisation is commonly carried out by introducing a constant pitch offset and evaluating its influence on aerodynamic performance across a range of operating conditions. This is typically implemented using blade-element or CFD-based frameworks, where the power coefficient and torque characteristics are mapped as functions of pitch angle and tip-speed ratio to identify favourable operating regimes [25, 26]. These studies show that the choice of fixed-pitch angle has a strong influence on stall onset, torque fluctuations, and overall aerodynamic efficiency [26].

Passive variable-pitch systems represent an intermediate class, in which the blade is allowed to rotate relative to the rotor through purely mechanical constraints rather than active control of the pitch angle. Such configurations have been shown to improve starting behaviour and aerodynamic performance while maintaining relatively simple mechanical design. Kirke and Paillard demonstrated that passive pitch mechanisms can achieve performance improvements by reducing adverse angles of attack during rotation [24]. These approaches retain the periodic nature of the aerodynamics but modify the instantaneous blade incidence in a way that partially alleviates stall and reduces cyclic loading. One such study, by Elkhoury et al, investigates the effect of a passive variable-pitch design, where the pitch is prescribed by the mechanism, and then is both experimentally and numerically tested to compare to the fixed-pitch case [27]. Whilst improvements are seen, a passive control mechanism would not allow for modified control strategies in changing wind conditions.

Active pitch control strategies extend this concept by prescribing the blade pitch as an explicit function of azimuth angle or operating state, and achieving these pitch angles using on-board actuators. In this framework, optimisation is carried out by tuning the pitch schedule to maximise aerodynamic performance or reduce unsteady loads. CFD-based studies of H-rotor turbines show that optimised pitch profiles can significantly enhance power extraction and improve flow attachment by mitigating dynamic stall effects [28]. Sensitivity analyses further demonstrate that performance is strongly dependent on the amplitude and phase of the pitch variation, indicating that relatively small changes in the control law can have a large impact on turbine behaviour [29]. Experimental and numerical investigations of actively controlled Darrieus turbines similarly show improvements in both starting torque and steady-state performance compared with fixed-pitch operation [30–33]. Delafin et al. use an active control strategy in only the upstream part of the turbine, where the angle of attack of the blades is bounded by a set angle, and this limiting angle is varied $(6°, 8°, 10°)$, with all three limits leading to a significant increase in power coefficient [34]. They do not consider the downstream part of the turbine, fixing the pitch angle at zero, since their expression for the angle of attack is based on a number of assumptions that are not valid for the downstream blades, overall requiring an undisturbed uniform velocity field.

Despite the similarities between these systems and the present work, several important differences remain. In the vertical-axis wind turbine literature, the primary objective is typically to maximise power extraction from the flow or overall turbine efficiency, which requires maximising the product of torque and angular velocity. In contrast, the present study focuses on maximising the torque generated by sails mounted on a large rotating flywheel, where the angular speed of the flywheel constrains the angular velocity of the sails. Furthermore, most modern investigations of variable-pitch turbines rely on detailed numerical aerodynamic models that incorporate effects such as dynamic stall, wake interactions, and flow separation. Here, we instead adopt a reduced-order quasi-steady model that enables analytical investigation of the optimal sail (or airfoil) orientation, under the assumption that the sails are significantly more spaced than the blades of a VAWT and as a first approximation we ignore wake interactions, turbulence, and downstream effects.

Accordingly, the present work may be viewed as complementary to the variable-pitch VAWT literature. Rather than providing a detailed numerical description of a specific turbine configuration and active-control, the aim is to develop analytical insight into the optimal orientation of a surface constrained to move along a circular trajectory, at all positions and for higher ranges of angles of attack. This simplified framework highlights how the optimal sail orientation depends on the relative magnitudes of the wind speed and rotational speed, and clarifies the role of orientation control in circular aerodynamic systems.

In this study, we therefore consider a simplified model of a sail moving along a circular trajectory under steady background wind conditions. The objective is to determine the optimal control of the sail's orientation in response to the continuously varying apparent wind experienced during rotation. Section 2 outlines the force model and derives the optimal orientation for a single sail using simplified lift and drag coefficients. Section 3 extends the analysis to multiple evenly spaced sails, then Section 4 uses experimental lift and drag coefficients from the NACA-0012 Airfoil [35] to compare with the results from the simplified model. Finally, Section 5 discusses physical considerations and limitations of the model.

2 Mathematical Formulation of the Problem

We characterise the sail by its angular position θ and its instantaneous velocity $\boldsymbol{V_s}$. As shown in Figure 2(a), we orient the coordinate axes such that the wind is blowing down the y-axis with velocity V_w, and $\theta = 0$ corresponds to the sail velocity $\boldsymbol{V_s}$ being directly into the wind. That is, we have

$$\boldsymbol{V_w} = -V_w \boldsymbol{j}, \tag{1}$$

$$\boldsymbol{V_s} = V_s(-\sin\theta \boldsymbol{i} + \cos\theta \boldsymbol{j}), \tag{2}$$

where V_w and V_s represent the magnitude of the wind and sail velocities respectively.

Another important concept is that of 'apparent wind', which is the wind that a moving object actually experiences. The apparent wind velocity is simply the wind from the reference frame of the sail and can therefore be found by subtracting the sail velocity from the wind velocity:

$$\boldsymbol{V_A} = \boldsymbol{V_w} - \boldsymbol{V_s} = V_s \sin\theta \boldsymbol{i} - (V_w + V_s \cos\theta)\boldsymbol{j}. \tag{3}$$

2.1 Forces on a Sail

In two dimensions, the force on the sail can be decomposed into its components perpendicular and parallel to the apparent wind, which are referred to as the lift force $\boldsymbol{F_L}$ and the drag force $\boldsymbol{F_D}$, respectively. These are shown in Figure 2(b), where we can see that, depending on the sizes of the lift and drag forces, as well as the apparent wind angle θ_A and sail offset angle σ, the resultant force from the wind $\boldsymbol{F_R} = \boldsymbol{F_L} + \boldsymbol{F_D}$ could have a positive component in the sail's direction of travel, even if the sail is moving partially into a headwind. This is similar to how a boat can sail upwind.

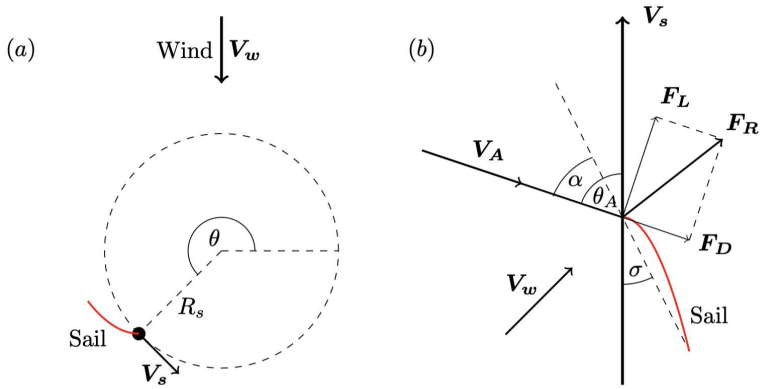


Fig. 2: (a) Plan view of a sail characterised by its angular position θ and velocity $\boldsymbol{V_s}$, at a distance R_s from the centre of rotation. (b) Plan view schematic of the forces on a sail, the apparent wind velocity $\boldsymbol{V_A}$ at angle θ_A, sail offset angle σ, and angle of attack $\alpha = \theta_A - \sigma$. (Oriented such that the sail velocity is directed upward.)

The magnitudes of the lift and drag forces on the sail have the same form, given by

$$F_L = \frac{1}{2}\rho c_L A V_A^2, \tag{4}$$

$$F_D = \frac{1}{2}\rho c_D A V_A^2, \tag{5}$$

where ρ is the density of the air, A is the cross-sectional area of the sail, V_A is the apparent wind speed, and c_D, c_L are the coefficients of drag and lift respectively. These coefficients are dependent on the angle of attack α which, as shown in Figure 2(b), is given by $\alpha = \theta_A - \sigma$. Note that, in this paper, we refer to the angle between the apparent wind velocity and the sail velocity as the apparent wind angle (θ_A), and the angle between the apparent wind velocity and the sail as the angle of attack ($\alpha = \theta_A - \sigma$). The dependence of the lift and drag coefficients on the angle of attack is empirical and would need to be determined for the specific sail or airfoil being employed. However, some approximations are used later to explore the behaviour of the sails, taking lift and drag data from a NACA airfoil [35]. The component of the resultant force, $\boldsymbol{F_R}$, in the direction of the sail velocity is given by

$$F_s = F_L \sin\theta_A - F_D \cos\theta_A, \tag{6}$$

where F_L and F_D are dependent on the angle of attack ($\alpha = \theta_A - \sigma$).

In the remainder of this section, we seek the optimal sail offset angle σ^* for each position θ that maximises the driving force in the direction of the sail velocity. This is equivalent to maximising the torque provided by the sail. In doing this, we are neglecting the effects of the perpendicular forces which may push the whole system downwind, since these are not considered useful.

2.1.1 Apparent Wind Angle

The first step to optimising the sail offset angle σ is to determine the apparent wind angle θ_A at any angular position θ. Since θ_A is the angle between the apparent wind and the sail velocity, we can determine θ_A using the cosine rule to get

$$\cos\theta_A = \frac{(-\boldsymbol{V_A})\cdot\boldsymbol{V_s}}{|\boldsymbol{V_A}||\boldsymbol{V_s}|} = \frac{V_s + V_w\cos\theta}{|\boldsymbol{V_A}|} = \frac{V_s + V_w\cos\theta}{\sqrt{V_s^2 + V_w^2 + 2V_wV_s\cos\theta}}. \tag{7}$$

Now, we need to consider when θ_A will be larger or smaller than π. Due to the wind direction being fixed in the negative y-direction, we can determine that the sign of $\theta_A - \pi$ depends on the sign of the x-component of the sail velocity (2). Therefore, we determine that $\theta_A \in [0,\pi]$ when $\sin\theta \leq 0$ ($\pi \leq \theta \leq 2\pi$) and, conversely, $\theta_A \in (\pi, 2\pi)$ when $\sin\theta > 0$ ($0 < \theta < \pi$). As such, we can write the apparent wind angle explicitly as

$$\theta_A(V_r,\theta) = \arccos\left(\frac{V_r + \cos\theta}{\sqrt{V_r^2 + 1 + 2V_r\cos\theta}}\right), \qquad \pi \leq \theta \leq 2\pi, \tag{8}$$

$$\theta_A(V_r,\theta) = 2\pi - \arccos\left(\frac{V_r + \cos\theta}{\sqrt{V_r^2 + 1 + 2V_r\cos\theta}}\right), \qquad 0 < \theta < \pi, \tag{9}$$

where $V_r = V_s/V_w$ is the ratio of the sail speed to wind speed, and is often termed the tip-speed ratio. We can see, therefore, that the apparent wind angle depends only on the relative sizes of the two speeds as well as the angular position of the sail. Figure 3 shows θ_A as a function of θ for multiple V_r values.

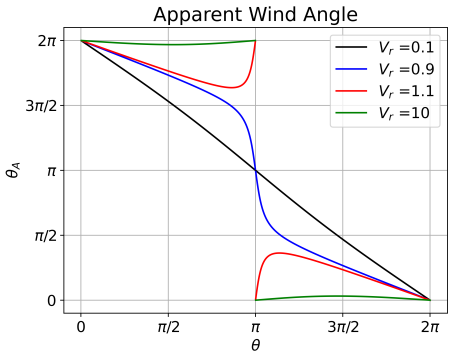


Fig. 3: The apparent wind angle θ_A vs the sail's angular position θ for multiple $V_r = V_s/V_w$ values.

Let us consider the limiting cases:

- $V_r \ll 1$: The sail speed is significantly lower than the wind speed. That is, the sail and rotating surface are almost stationary compared to the wind. In this case

$$\theta_A \sim 2\pi - \theta + V_r \sin\theta + \mathcal{O}(V_r^2).$$

  In the limit $V_r \to 0$, we have $\theta_A \to 2\pi - \theta$, where the apparent wind and 'true wind' become the same.
- $V_r \to \infty$: The wind speed is significantly lower than the sail speed. In this case

$$\theta_A \sim \begin{cases} -\frac{\sin\theta}{V_r}, & \pi \le \theta \le 2\pi, \\ 2\pi - \frac{\sin\theta}{V_r}, & 0 < \theta < \pi, \end{cases} + \mathcal{O}\left(V_r^{-2}\right).$$

  Approximately, we have $\theta_A \approx 0$ or 2π, since the apparent wind is simply due to the velocity of the sail itself, and therefore the sail will experience a headwind.
- $V_r = 1$: The wind speed and sail speed are equivalent.

$$\theta_A = \begin{cases} \pi - \frac{\theta}{2}, & \pi \le \theta \le 2\pi, \\ 2\pi - \frac{\theta}{2}, & 0 < \theta < \pi. \end{cases}$$

  The apparent wind angle varies linearly with position, with a discontinuity at $\theta = \pi$, where the apparent wind vanishes and the angle jumps by 180°. This is the only non-trivial case where the magnitude of the apparent wind V_A can be zero, occurring only at $\theta = \pi$.

From Equations (8) and (9), we can also determine when a sail moves downwind with respect to the apparent wind, that is, when $\pi/2 < \theta_A < 3\pi/2$. This will occur if and only if the argument of the arccos expression is negative, which corresponds to

$$V_r < -\cos\theta. \tag{10}$$

Hence, the apparent wind can only be behind the sail if $0 \le V_r < 1$ and $\frac{\pi}{2} < \theta < \frac{3\pi}{2}$. This can be seen in Figure 3, where for $V_r > 1 (V_r = 1.1, 10)$ θ_A is never in $[\pi/2, 3\pi/2]$ and thus the sail never experiences a tailwind. However, for $V_r < 1 (V_r = 0.1, 0.9)$ we can see in the figure that there is a continuous interval for $\theta \in (\pi/2, 3\pi/2)$ where the sail feels an apparent tailwind. The length of this interval for θ is dependent upon V_r, where a lower V_r will have a longer interval experiencing a tailwind compared with a higher V_r.

2.2 Effect of Asymmetry of Sail

The sails used could be either flexible (invertible) sails, similar to that on a boat where the sails can bend with respect to the wind direction, or they could be rigid like an airfoil, where the curvature is fixed. The type of sail is important as some will possess 180-degree rotational symmetry, like a rectangular sail or flat plate, whereas others will not, such as most airfoils or even most sails used on sailing boats. This has an effect on the continuity of the optimal σ values, which will be shown in Section 2.4. In order to make progress, we will assume that the sail is not rotationally symmetric, but recognise

that certain discontinuities in σ could be resolved with a rotationally symmetric sail. It is important to note that it is rotational symmetry that is required to remove these discontinuities; an airfoil with no camber (which has reflective symmetry) does not have to be rotationally symmetric (for example, Figure 5(c)). The terms "symmetric" and "asymmetric" from hereon refer to rotational symmetry.

In the next section, we find it necessary to place bounds on σ for an asymmetric sail, since the approximate forms of the lift and drag coefficients we use are symmetric. To do this, we impose that the lift force has a positive component in the direction of the sail velocity and that the wind is always blowing into the same side of the sail. This is shown diagrammatically in Figure 4, where the apparent wind is always blowing into the concave side of the sail. We note that the figure shows a cambered sail/airfoil, but these bounds would also apply to a zero-camber airfoil that does not possess rotational symmetry (like Figure 5(c)). We can ascertain from Figure 4 the

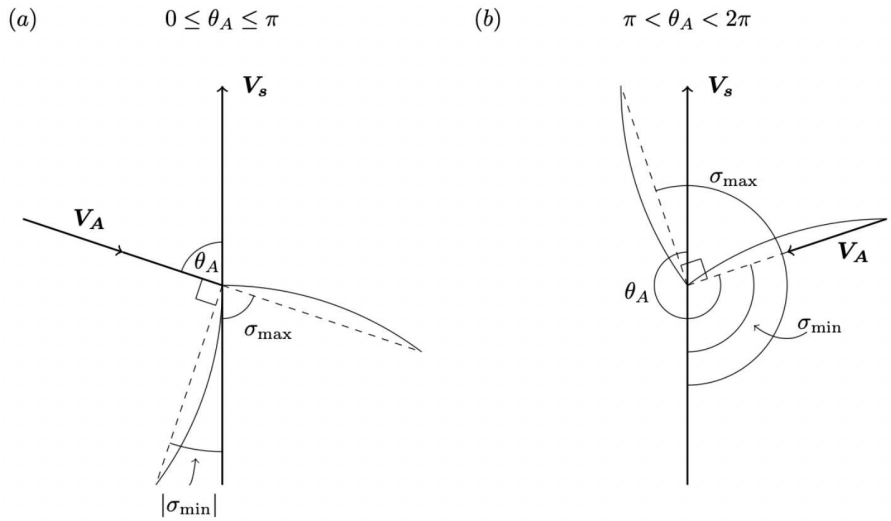


Fig. 4: The minimum and maximum σ values in our optimisation constraint for both (a) $0 \leq \theta_A \leq \pi$ and (b) $\pi \leq \theta_A < 2\pi$.

following bounds:

$$0 \leq \sigma \leq \theta_A, \quad \text{or} \quad \theta_A + \frac{3\pi}{2} \leq \sigma \leq 2\pi : \qquad 0 \leq \theta_A < \frac{\pi}{2}, \tag{11}$$

$$\theta_A - \frac{\pi}{2} \leq \sigma \leq \theta_A : \qquad \frac{\pi}{2} \leq \theta_A \leq \pi, \tag{12}$$

$$\theta_A - \pi \leq \sigma \leq \theta_A - \frac{\pi}{2} : \qquad \pi < \theta_A < 2\pi. \tag{13}$$

These bounds are used in the numerical calculations to solve for the optimal σ, however, it is worth noting that with lift and drag coefficients for an asymmetric sail,

these bounds would not need to be used as the asymmetrical lift and drag coefficients should place the optimal σ within these bounds anyway.

2.3 Determining the Optimal Sail Offset Angle

Let us denote the optimal sail offset angle by σ^*. We seek the optimal sail offset angle by maximising F_s in (6), the force in the direction of the sail velocity. This is equivalent to maximising the torque from the sail. Combining the expressions in Equations (4), (5), and (6), we know that

$$F_s = \frac{1}{2}\rho A V_A^2 \left[c_L(\theta_A - \sigma)\sin\theta_A - c_D(\theta_A - \sigma)\cos\theta_A\right], \tag{14}$$

where $c_L(\theta_A - \sigma), c_D(\theta_A - \sigma)$ are the lift and drag coefficients as functions of the angle of attack, $\alpha = \theta_A - \sigma$.

Since θ_A is a function of θ and V_r, the optimal σ will depend not only on the sail's position but also the relative wind speed, as expected. The $\frac{1}{2}\rho A V_A^2$ coefficient in Equation (14) is always going to be a positive constant whose magnitude is independent of σ (see (3)), and therefore we can focus on maximising the expression inside the square brackets to determine σ^*. As such, we define the objective function

$$g(\sigma, V_r, \theta) = c_L(\theta_A - \sigma)\sin\theta_A - c_D(\theta_A - \sigma)\cos\theta_A, \tag{15}$$

where $\theta_A = \theta_A(\theta, V_r)$. Then, we solve the problem

$$\sigma^*(V_r, \theta) = \arg\max_{\sigma \in B} g(\sigma, V_r, \theta), \tag{16}$$

where B are the bounds for σ given in (11), (12) and (13).

2.3.1 Lift and Drag Coefficients

The calculations in the rest of this paper make use of the following expressions for the lift and drag coefficients:

$$c_L(\alpha) = a\sin 2\alpha, \tag{17}$$

$$c_D(\alpha) = b\sin^2\alpha + d. \tag{18}$$

These forms of lift and drag coefficients have π-periodicity and therefore it is important that we use the bounds on σ stated previously.

To approximate lift and drag coefficients, we could consider elastic collisions between the air molecules and a flat sail (or plate). In this case, the lift and drag coefficients would be given by

$$c_L(\alpha) \propto \sin 2\alpha, \quad c_D(\alpha) \propto \sin^2\alpha. \tag{19}$$

In reality, the drag will never be zero even when the sail is aligned to be as streamlined as possible, which can be seen in various experimental results [35–37]. As such,

the additive shift of the drag coefficient was included to arrive at (18). This elastic collision model matches quite well with post-stall regimes such as those determined experimentally by Sandia National Laboratory testing seven different (reflectively) symmetrical NACA airfoil sections [35]. However, it does underestimate the lift at smaller angles of attack. This may suggest that the optimal σ values calculated in this section are slightly smaller than they should be. However, later in Section 4, we show how to resolve this using experimental lift and drag coefficients.

A potential flow formulation was considered as a possible route to obtain analytical lift expressions, however, such an approach leads to a lift behaviour that is qualitatively different at larger angles of attack from the experimentally observed coefficients used in this work, in particular predicting a maximum lift magnitude near $\alpha = 90°$ [38], whereas experimental data (e.g. the NACA-0012 Airfoil in Figure 5) shows lift decreases to zero at $\alpha = 90°$, as would be expected. In addition, while CFD could provide further insight into the flow physics, accurately predicting separated flows over the full range of angles of attack considered here would require a substantially more detailed modelling approach. Since the focus of this work is the optimisation of the sail motion and orientation rather than detailed flow prediction, we believe that using experimentally measured lift and drag coefficients provides the most appropriate balance between physical fidelity and model simplicity.

As an example, Figure 5 shows graphs of the lift and drag coefficients of the NACA-0012 Airfoil, with data taken from [35], overlain with the approximating sinusoidal lift and drag coefficients from (17), (18), taking $a = 1, b = 1.7, d = 0.1$. The NACA-

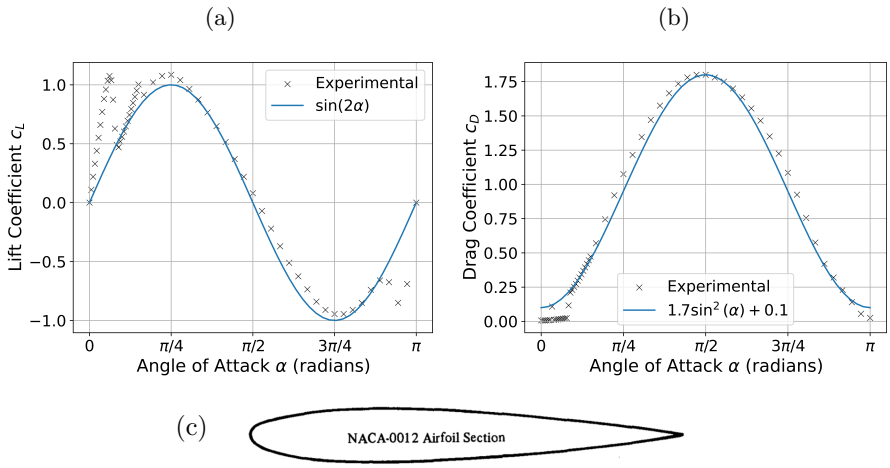


Fig. 5: Experimental (a) lift and (b) drag coefficients for the NACA-0012 Airfoil [35], with $c_L(\alpha) = \sin(2\alpha)$ and $c_D(\alpha) = 1.7\sin^2\alpha + 0.1$ overlain in blue. The shape of the NACA-0012 Airfoil is shown in (c).

0012 Airfoil is an example of an airfoil that has no camber and possesses reflective symmetry along its long axis, yet does not have rotational symmetry. This can be seen

in the experimental data in Figure 5(a) where the magnitude of the lift coefficient is larger at $\alpha = \pi/4$ compared to $\alpha = 3\pi/4$. This is not captured by the sinusoidal lift and drag coefficients, and hence why the bounds can be required for airfoils with no camber, if they are not rotationally symmetric.

2.4 Results for a Single Sail

Using the lift and drag coefficients (17) and (18) within (16), the values for σ^* were calculated for varying θ and V_r values. These are shown in Figure 6. For $V_r < 1$, we can see that there is a single discontinuity at $\theta = 0, 2\pi$, which corresponds to the point where the sail is travelling directly into the headwind. As mentioned previously, this discontinuity does not exist for a rotationally symmetric sail and is therefore only applicable for an asymmetric one. Additionally, as one might expect, we see that the optimal sail offset angle is perpendicular to the wind at $\theta = \pi$, where maximising the drag force is most advantageous when sailing with a tailwind. In contrast, for

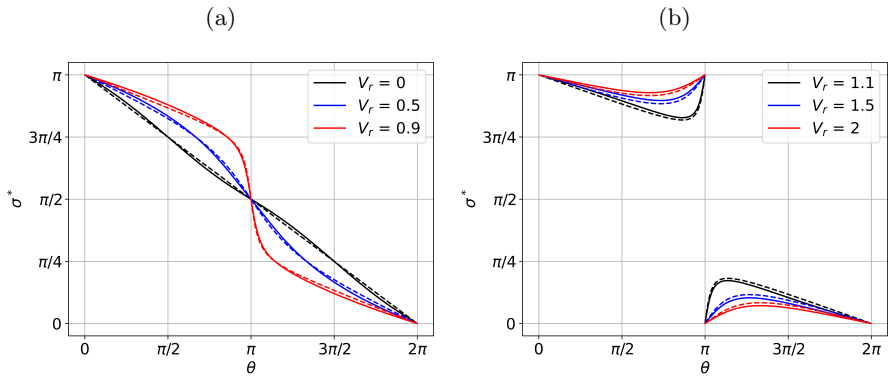


Fig. 6: The optimal sail offset angles σ^* for (a) $V_r < 1$ and (b) $V_r > 1$. The dashed lines are given by $\sigma^* = \theta_A/2$ (35), which is the exact solution for $2a = b$.

$V_r > 1$, there are two noticeable differences. The first is that the magnitudes of the sail offset angles tend to 0 and π, as V_r increases. This is due to the apparent wind angle decreasing as V_r increases, and therefore the sail offset also decreases to compensate. The other difference is that there are two discontinuities in σ^* for $V_r > 1$, at $\theta = 0$ and $\theta = \pi$. This extra discontinuity arises due to the sail now experiencing a headwind instead of a tailwind as it passes through $\theta = \pi$, in which case the behaviour is similar to that at $\theta = 0$. Therefore, in this model a symmetric sail would be preferred, especially when rotating at higher speeds, in order to avoid these discontinuities.

Figures 7 and 8 show a single sail at its optimal offset angles at various positions around the circle, effectively providing snapshots through time. For $V_r < 1$ (Figure 7), the sail follows a smooth rotation, with streamlined orientations on the windward side ($0 \leq \theta \leq \pi/2$ and $3\pi/2 \leq \theta \leq 2\pi$) and broader orientations on the leeward side, consistent with the behaviour predicted by Figure 6. In contrast, for $V_r > 1$ (Figure

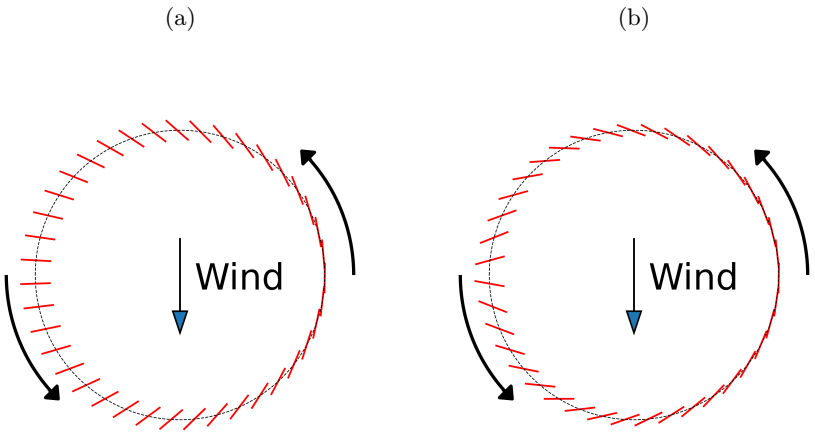


Fig. 7: A single sail at its optimal offset angles through snapshots in time for (a) $V_r = 0.1$ and (b) $V_r = 0.9$.

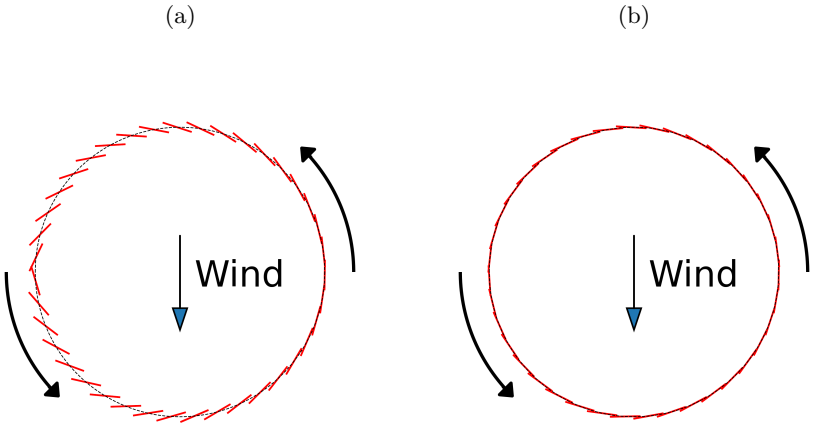


Fig. 8: A single sail at its optimal offset angles through snapshots in time for (a) $V_r = 1.1$ and (b) $V_r = 10$.

8), the sail orientations tend to align more closely with the apparent wind for most of the rotation, particularly on the leeward side ($\pi/2 < \theta < 3\pi/2$), reflecting the reduced optimal offset angles at higher speeds. The main difference between these two regimes is that, for $V_r < 1$, the sail maximises drag near $\theta = \pi$, whereas for $V_r > 1$ this effect is diminished. What is not visible in these snapshots, but is evident in the graphs of

σ^* versus θ (Figure 6), are the discontinuities at $\theta = 0$ and $\theta = \pi$. As mentioned earlier, these discontinuities arise from rotationally asymmetric sails, however, the figures represent the sail as a straight line, effectively showing the smooth trajectory corresponding to a rotationally symmetric sail.

Since the optimal sail offset angle, $\sigma^*(V_r, \theta)$, can be calculated at any position given the sail and wind speeds, we can determine the optimal driving force, and therefore torque, generated by a single sail as it rotates. Scaling the torque with the square of the wind speed and other constant terms, we get the following expression for the optimised dimensionless torque,

$$\begin{aligned}\tau^* &= \frac{2\tau}{\rho A R_1 V_w^2} = \frac{2R_s F_s(\sigma^*)}{\rho A R_1 V_w^2}, \\ &= \frac{R_s}{R_1}\left(V_r^2 + 1 + 2V_r\cos\theta\right)\left(c_L(\theta_A - \sigma^*)\sin\theta_A - c_D(\theta_A - \sigma^*)\cos\theta_A\right), \end{aligned} \tag{20}$$

where $\tau^* = \tau^*(V_r, \theta)$ is the dimensionless optimised torque, R_1 is a reference radius (for example, the outer radius of the flywheel), and R_s is the radius at which the sails are placed. R_1 is used as the reference radius to allow for analysis of finding the optimal R_s value. This is plotted against θ for multiple V_r values in Figure 9. We can see that the

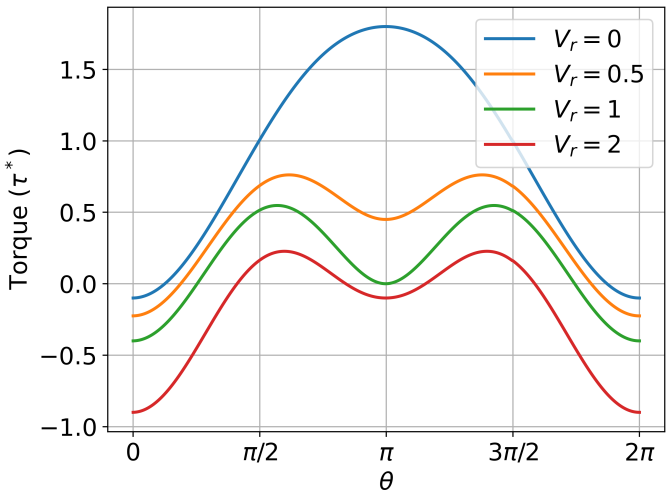


Fig. 9: The dimensionless optimised torque generated by a single sail (with $R_s = R_1$).

most effective positions are generally close to $\theta = \pi/2$ and $\theta = 3\pi/2$, which correspond to where the sail is travelling perpendicular to the wind direction. This result is to be expected given that the direction for sailing fastest in a boat is perpendicular to the wind [39]. Additionally, we can see that the torque generated is symmetric about $\theta = \pi$. That is, the torque generated depends only on the x-coordinate of the sail, since the wind is blowing directly down the y-axis.

2.4.1 Further Analytical Progress

Here, we consider further analytical progress that can be made using sinusoidal lift and drag coefficients given in (17) and (18), for arbitrary a, b, d. In particular, we consider the relationship between σ^* and θ_A in the asymptotic limit that the lift and drag forces are imbalanced.

We seek a turning point of $g(\sigma, V_r, \theta)$ (in terms of σ), which satisfies

$$c_L'(\theta_A - \sigma^*)\sin\theta_A = c_D'(\theta_A - \sigma^*)\cos\theta_A. \tag{21}$$

Using the lift and drag coefficients along with (21), we arrive at

$$\frac{2a}{b}\tan\theta_A = \tan\left(2\left(\theta_A - \sigma^*\right)\right), \quad \cos\theta_A \neq 0. \tag{22}$$

If we consider the two specific θ_A values where the apparent wind velocity is perpendicular to the sail velocity (and therefore $\cos\theta_A = 0$), we can determine that

$$\sigma^*\left(\theta_A = \frac{\pi}{2}\right) = \frac{\pi}{4}, \tag{23}$$

$$\sigma^*\left(\theta_A = \frac{3\pi}{2}\right) = \frac{3\pi}{4}. \tag{24}$$

These two values for σ^* correspond to maximising the lift force without considering the drag forces. This is because, in this model the forces perpendicular to the torque are ignored, and $\cos\theta_A = 0$ corresponds to the drag being directly perpendicular to the direction of travel of the sail.

We now consider the case when $\cos\theta_A \neq 0$, and rearrange Equation (22) for σ^* to arrive at

$$\sigma^* = \theta_A + \frac{k\pi}{2} - \frac{1}{2}\arctan\left(\frac{2a}{b}\tan\theta_A\right), \quad k \in \mathbb{Z}. \tag{25}$$

A complication herein lies with determining k as a function of θ_A such that the bounds (11) - (13) are satisfied. The value that $k(\theta_A)$ takes is also dependent upon a and b. Thus, we consider the asymptotic limits of the term inside the arctan argument where $k(\theta_A)$ can be determined explicitly.

We first consider the case when the drag force is much larger than the lift force. This can be either due to the relative size of b compared to a ($b \gg a$), or the apparent wind angle is close to a headwind or tailwind ($\theta_A \to 0, \pi$). In either case, we can take an asymptotic approach and let

$$\frac{2a}{b}\tan\theta_A = \epsilon, \quad |\epsilon| \ll 1. \tag{26}$$

This gives the asymptotic expansion

$$\sigma^* \sim \theta_A + \frac{k\pi}{2} - \frac{a}{b}\tan\theta_A + \frac{4a^3}{3b^3}\tan^3\theta_A + \mathcal{O}\left(\epsilon^5\right). \tag{27}$$

Using $\sigma^* = \theta_A + \frac{k\pi}{2} + \mathcal{O}(\epsilon)$ and the bounds (11), (12), (13), we can easily determine that

$$k = \begin{cases} 0, & 0 \le \theta_A < \frac{\pi}{2}, \\ -1, & \frac{\pi}{2} \le \theta_A \le \frac{3\pi}{2}, \\ -2, & \frac{3\pi}{2} \le \theta_A < 2\pi, \end{cases} \tag{28}$$

to give

$$\sigma^* = \begin{cases} \theta_A, & 0 \le \theta_A < \frac{\pi}{2}, \\ \theta_A - \frac{\pi}{2}, & \frac{\pi}{2} \le \theta_A \le \frac{3\pi}{2}, \\ \theta_A - \pi, & \frac{3\pi}{2} \le \theta_A < 2\pi, \end{cases} + \mathcal{O}(\epsilon), \tag{29}$$

where the higher order terms are the same as in Equation (27). This simply tells us that if drag forces are significantly more important than lift forces, then, if the sail is travelling into the apparent wind ($0 \le \theta_A < \frac{\pi}{2}$ or $\frac{3\pi}{2} < \theta_A < 2\pi$), the sail should be streamlined to minimise the drag by having the angle of attack ($\alpha = \theta_A - \sigma$) close to zero. Conversely, if the sail is travelling with the apparent wind $\left(\frac{\pi}{2} \le \theta_A \le \frac{3\pi}{2}\right)$, then the angle of attack should be close to $\pi/2$ so that the sail is perpendicular to the apparent wind and can maximise the drag force.

We now consider the opposite case, where the lift force is significantly more important than the drag force, either due to an imbalance in the size of b compared to a ($a \gg b$), or the apparent wind angle is close to perpendicular to the direction of travel of the sail ($\theta_A \to \pi/2, 3\pi/2$). In this case, we also consider an asymptotic approach, where we take

$$\frac{2a}{b}\tan\theta_A = \frac{1}{\epsilon}, \quad |\epsilon| \ll 1. \tag{30}$$

This gives the asymptotic expansion

$$\sigma^* \sim \theta_A + \frac{\pi}{4}(2k-1) + \frac{b}{4a}\cot\theta_A - \frac{b^3}{48a^3}\cot^3\theta_A + \mathcal{O}(\epsilon^5). \tag{31}$$

The values for k here, however, are different depending upon θ_A,

$$k = \begin{cases} 0, & 0 \le \theta_A < \pi, \\ -1, & \pi \le \theta_A < 2\pi, \end{cases} \tag{32}$$

which gives

$$\sigma^* = \begin{cases} \theta_A - \frac{\pi}{4}, & 0 \le \theta_A < \pi, \\ \theta_A - \frac{3\pi}{4}, & \pi \le \theta_A < 2\pi, \end{cases} + \mathcal{O}(\epsilon), \tag{33}$$

where the higher order terms are the same as in Equation (31). This shows that the sail will be maximising the lift force by being approximately 45 degrees offset to the apparent wind.

2.4.2 $2a = b$

The optimal sail offset angle simplifies greatly for the specific case when $2a = b$. While quite specific, this case is not too far from our approximation for the NACA-0012 airfoil shown in Figure 5, which we are approximating with $a = 1, b = 1.7$.

In the specific case that $2a = b$, we have from (25) that

$$\sigma^* = \frac{\theta_A}{2} + \frac{k\pi}{2}, \quad k \in \mathbb{Z}, \tag{34}$$

where using the bounds (11) - (13) determines $k = 0$, for all θ_A. That is, the optimal sail angle in the case that $2a = b$ is simply half the apparent wind angle:

$$\sigma^* = \frac{\theta_A}{2}. \tag{35}$$

This is plotted in Figure 6 as the dashed lines, where we see quite close agreement to the numerical results with $a = 1, b = 1.7$.

3 Multiple Sails

Next, we consider a generalisation to the case of multiple sails. For simplicity, we consider evenly spaced sails around a circle and make the key assumption that the sails do not interact or interfere with each other and can therefore be optimised independently. Therefore, a number of evenly spaced sails optimised individually at a single moment in time would appear the same as for a single sail at different moments in time. That is, Figures 7 and 8 are equivalent to the orientation of 40 evenly spaced sails at a particular moment in time.

In reality, with 'closely' spaced sails, the interaction between the sails would cause this model to break down. This interaction between closely spaced sails is considered in [40] for two sails on the same ship, and in [41] for two ships sailing close to each other. As the upwind sails 'shield' the sails that are further downwind, the downwind sails would be heading more into a headwind due to their velocity, and therefore those sails would need to have a smaller σ value than calculated for a single sail, and overall would be less advantageous to generating torque. Additionally, the wind would be more turbulent for the downwind sails, affecting their performance as well. This is a common problem with wind turbines as well. For example, a spacing of 10 rotor diameters can decrease power output by more than twenty-percent, with still a ten-percent decrease in power output at 28 rotor diameters apart [42, 43]. The distance D between N evenly spaced sails is given by

$$D = 2R_S \sin\frac{\pi}{N} \approx \frac{2\pi R_S}{N}, \quad N \gg 1. \tag{36}$$

Thus, the number of sails must be carefully chosen dependent with respect to their size and shape in order to limit the effects between them. For instance, if we bound (36) by n sail widths ($D > nD_S$), then we find $N < 2\pi R_S/nD_S$.

The total (dimensionless) torque produced by N evenly spaced sails is given by

$$\tau_{\mathrm{TOT}}(V_r, \theta) = \sum_{k=0}^{N-1} \tau^*(V_r, \theta + \frac{2\pi k}{N}), \tag{37}$$

where θ denotes the angular position of any one sail—due to the uniform spacing, the total torque is independent of which sail is chosen as the reference. By numerically calculating τ_{TOT} over $\theta \in [0, 2\pi]$, we can determine how variable the wind power is depending on N, where we expect the total torque to be periodic over a range of $2\pi/N$. The plots in Figure 10 show τ_{TOT} for both four and twelve sails, at different relative rotational speeds. We can see that, not only does the periodicity reduce as N

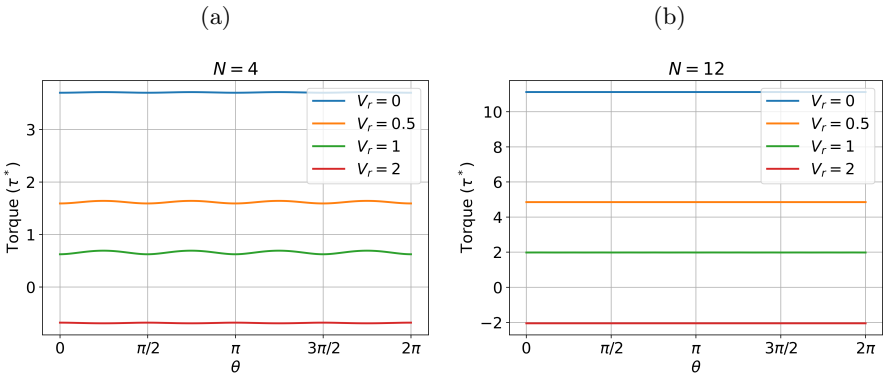


Fig. 10: The (dimensionless) torque (37) generated by (a) $N = 4$ and (b) $N = 12$ sails for multiple V_r values.

increases, but so too does the variance of the total torque produced. The variance is almost imperceptible for $N = 12$ in relation to the magnitude of the torque, and we can accurately approximate the total torque by its average value. As the number of sails increases, the sum over the sails approaches the number of sails multiplied by the average output of each sail over a whole rotation. That is, we can approximate the dimensionless torque from N sails as

$$\bar{\tau}_{\mathrm{TOT}}(V_r) \approx \frac{N}{2\pi} \int_0^{2\pi} \tau^*(V_r, \theta)\, \mathrm{d}\theta. \tag{38}$$

3.1 Dependence on Angular Velocity

We may also be interested in the dependence of the wind torque on the angular velocity of the sails (and flywheel) ω. This establishes itself in the dependence on V_r, since, for

a given wind speed and sail radius, the angular velocity is proportional to V_r:

$$V_r = \frac{V_s}{V_w} = \frac{\omega R_s}{V_w}. \tag{39}$$

Figure 11 shows the dependence of the torque on V_r, where we can see that not only is the torque proportional to N, but also that the sails start counteracting the rotation of the device at some critical value V_{r0}, which is approximately 1.5 in this case. This suggests that the operational angular velocity should not often exceed 1.5 times the wind velocity divided by the sail radius. However, this value of V_{r0} at which the sails become a hindrance is sensitive to the lift and drag coefficients.

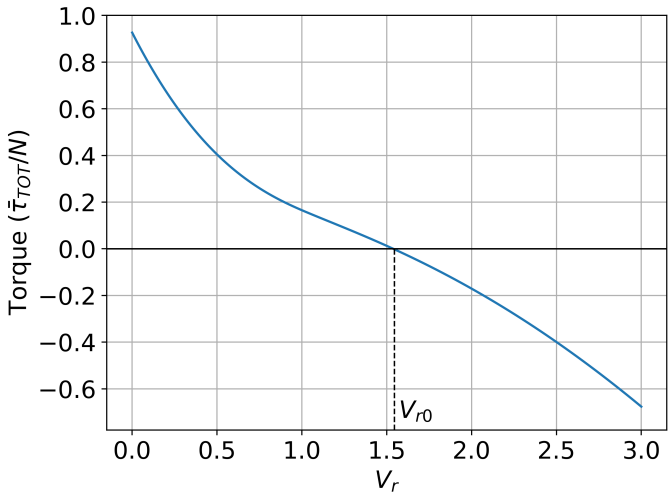


Fig. 11: The dimensionless mean torque ($\bar{\tau}_{\mathrm{TOT}}$) (38) scaled by N, as a function of V_r, given the sail radius is constant. Since the sails are assumed to be non-interacting, the mean total torque from N sails divided by N is simply the average torque produced from one sail over a full revolution.

In fact, increasing the drag coefficient will result in a decrease in the value of V_{r0}. This is shown in Figure 12, where V_{r0} is plotted against b and d with $c_D = b\sin^2\alpha + d$. In both cases, an increase in the drag coefficient results in a decrease in V_{r0}. For $d = 0$, the torque is always positive as the drag can always be reduced to zero, and thus the sails never become a hindrance (i.e. $V_{r0} \to \infty$). However, for $d > 0$, this is not possible as the hindrance due to the drag can never be completely removed, and at high enough speeds the detrimental drag will dominate any gains from lift. Thus, accurate lift and drag coefficients are important in determining the operating limits for useful sails.

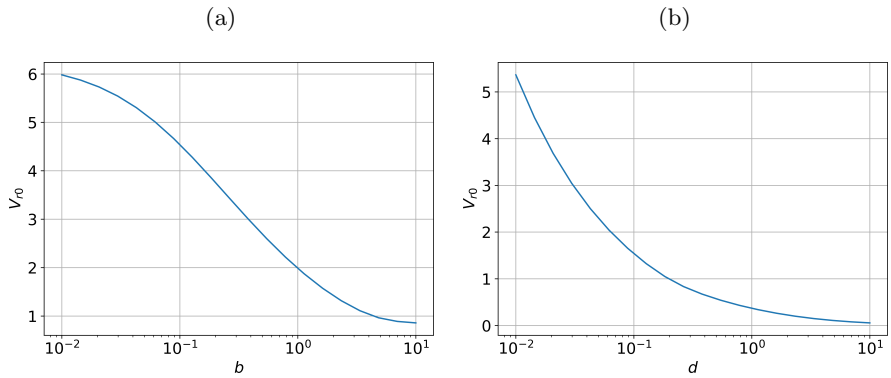


Fig. 12: The critical rotation speed V_{r0} versus (a) b for $c_D(\alpha) = b\sin^2\alpha + 0.1$, (b) d for $c_D(\alpha) = 1.7\sin^2\alpha + d$.

3.2 Dependence on Sail Radius

The previous work assumes that the sails are at some sail radius R_s from the centre of rotation. The choice of R_s is restricted by the size and shape of the setup. However, for a given angular velocity and wind speed, the dependence of F_s on R_s (14) is the same as the dependence on V_r given in Section 3.1, since $V_r = \omega R_s/V_w$. Therefore, the force will be a monotonically decreasing function of R_s, which may at first suggest to have the sails as close to the inner edge as possible. This is true for maximising the force provided by the sails, since it reduces the tangential velocity of the sails. However, the torque is proportional to the product of the sail radius and the force. Therefore, it is not trivial that the sails should be placed at either the innermost or outermost edge. In fact, we find there is a single radius that maximises torque for a given $\omega > 0$.

Figure 13 shows the dimensionless torque produced from 12 sails as a function of R_s/R_1. Each curve represents a different ratio of angular velocity to wind velocity, where $\omega R_1/V_w = V_r R_1/R_s$ is an analogue to V_r but for a constant reference radius R_1—the outer radius of the flywheel—since R_s is being varied. We can see that for higher operating angular velocities, the maximum torque will come from a smaller R_s, whereas, conversely, for lower angular velocities, the sails would be more effective placed closer to the outer edge.

If we consider the mean torque as a function of just the sail radius and angular velocity, with all other parameters held constant, we can write

$$\tau(\omega, R_s) = R_s F(V_r(\omega, R_s)), \quad V_r = \frac{\omega R_s}{V_w},$$

where the force $F(V_r)$ is a monotonically decreasing function of the tip-speed ratio V_r. In Section 3.1, it was seen that the torque is a decreasing function of ω for a constant sail radius, which naturally holds since the torque is a constant multiple of the force given a constant sail radius. If we instead consider a constant angular velocity, then

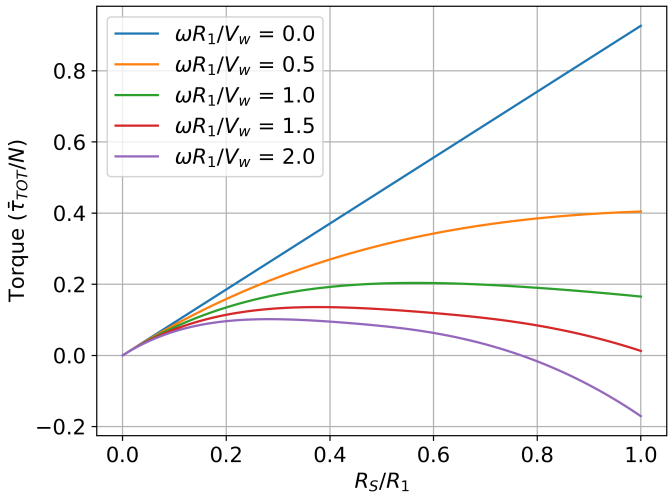


Fig. 13: The dimensionless mean torque (38) scaled by N, as a function of the dimensionless sail radius.

the optimal sail radius R_s^* gives

$$\left.\frac{\partial \tau}{\partial R_s}\right|_{R_s=R_s^*} = F(V_r^*) + V_r^* F'(V_r^*) = 0, \tag{40}$$

where $V_r^* = \omega R_s^*/V_w$ is the optimal tip-speed ratio. Since V_r^* is solved for implicitly through (40), with no explicit dependence on either the sail radius or angular velocity, this optimal tip-speed ratio is true for any angular velocity, with the optimal sail radius given by

$$R_s^* = \min\left\{\frac{V_w V_r^*}{\omega}, R_1\right\}.$$

This constrains the sail to being placed on the flywheel, since R_1 is the outer radius of the flywheel. Hence, the optimal sail radius is inversely proportional to the angular velocity, limited by R_1. This is seen in Figure 14. The particular value of V_r^* that solves (40) in this case is approximately $V_r^* \approx 0.566$.

3.3 Radial Forces

So far, we have only discussed the component of force in the direction of the sail velocity, as this is the component that will provide the torque we wish to maximise. However, each sail will also provide a component of force that is perpendicular to the rotation and acting radially with respect to the rotating device. The magnitude of this

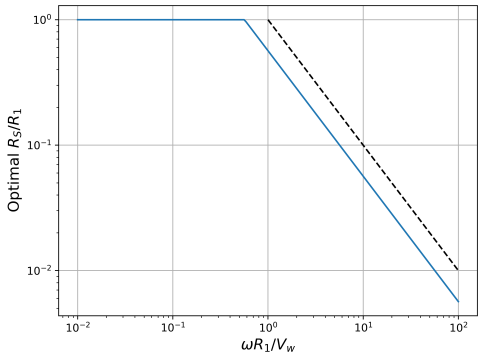


Fig. 14: Dimensionless plot of the optimal sail radius R_s^* as a function of angular velocity ω. The dashed black line represents inversely proportional behaviour.

radial force is given by

$$\begin{aligned} F_{\mathrm{RAD}} &= F_L \cos\theta_A + F_D \sin\theta_A, \\ &= \frac{1}{2}\rho A V_A^2 \left(c_L(\theta_A - \sigma^*)\cos\theta_A + c_D(\theta_A - \sigma^*)\sin\theta_A\right), \end{aligned} \tag{41}$$

or, nondimensionalising,

$$\hat{F}_{\mathrm{RAD}} = \frac{2F_{\mathrm{RAD}}}{\rho A V_w^2} = (V_r^2 + 1 + 2V_r\cos\theta)\left(c_L(\theta_A - \sigma^*)\cos\theta_A + c_D(\theta_A - \sigma^*)\sin\theta_A\right), \tag{42}$$

where $\hat{F}_{\mathrm{RAD}}$ is a dimensionless force term and the direction of this radial force is 90 degrees clockwise of the sail velocity. Therefore, the radial force from a single sail is in the direction $\cos\theta\boldsymbol{i} + \sin\theta\boldsymbol{j}$.

The magnitude of the radial force as a function of θ is shown in Figure 15(a). The force reaches its largest magnitude when the sail moves approximately perpendicular to the wind ($\theta \approx \pi/2, 3\pi/2$). This behaviour is consistent with expectations when maximising the torque: when the sail travels directly with or against the wind, the drag force is either maximised or minimised, causing the radial component—the lift force—to vanish.

From this figure, we also observe that $\hat{F}_{\mathrm{RAD}}$ is an odd function about $\theta = \pi$. The force in the x-direction—perpendicular to the wind—is given by $\hat{F}_{\mathrm{RAD}}\cos\theta$, which is likewise odd about $\theta = \pi$. Consequently, the net force in the x-direction from a sufficient number of evenly spaced sails would cancel out. In contrast, the force in the wind direction is given by $\hat{F}_{\mathrm{RAD}}\sin\theta$, shown in Figure 15(b). This component is even about $\theta = \pi$, meaning that the net force from multiple sails (or the total output from a single sail completing a full rotation at constant angular velocity) acts to push the flywheel downwind. This resultant downwind force would therefore need to be

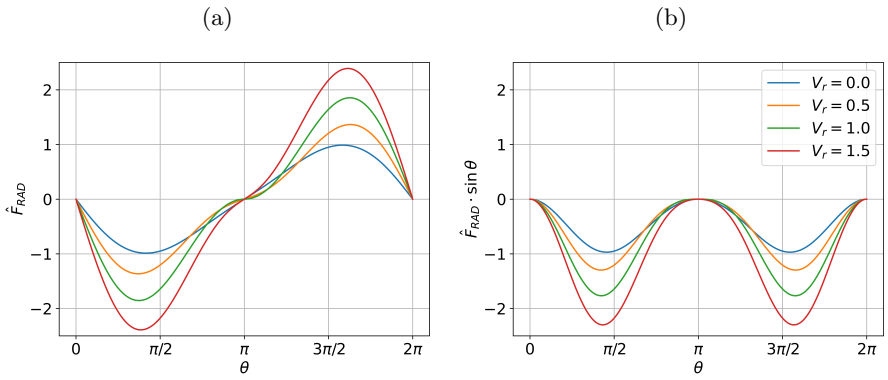


Fig. 15: (a) The magnitude of the radial force from a single sail $\hat{F}_{\mathrm{RAD}}$ (42) and (b) the component of the radial force from a single sail that is in the direction of the wind, $\hat{F}_{\mathrm{RAD}} \sin\theta$.

counterbalanced by another mechanism to hold the device in position if required—such as with *Gyrerg*.

4 Results With Experimental Coefficients

In this section, we show the results for σ^* using a cubic spline interpolation of the experimental data for lift and drag coefficients. The interpolants are shown in Figure 16.

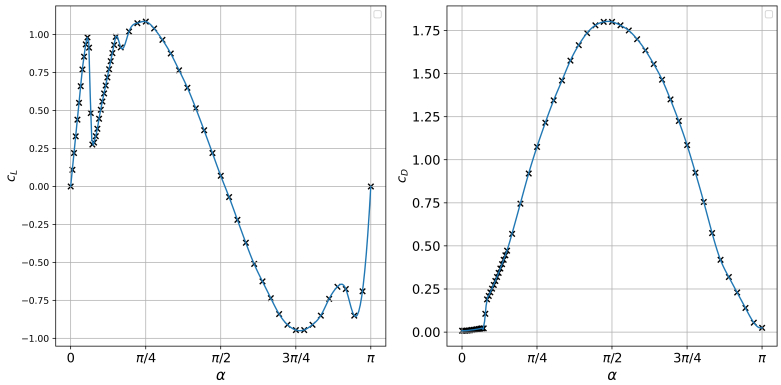


Fig. 16: The experimental data for lift and drag coefficients of the NACA-0012 Airfoil [35], with cubic spline interpolants overlain.

We seek to understand and emphasise the differences between the optimal sail offset angles using the experimental data compared to those calculated using the

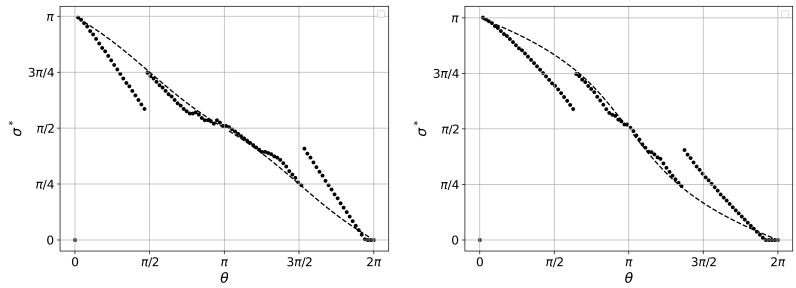


Fig. 17: The optimal sail offset angle σ^* vs position θ using the experimental lift and drag coefficients, with the simple sinusoidal model result shown as the dashed line. (Left) $V_r = 0$, (Right) $V_r = 0.5$.

simple sinusoidal model already presented. Comparing the lift and drag coefficients (in Figure 5), the main difference is at small angles of attack, where the simple sinusoid significantly underestimates the lift coefficient in the pre-stall region. Just from this observation, we expect that when the sail is travelling into the wind, where lift is to be maximised and drag minimised, that the optimal sail offset angle will place the angle of attack in the pre-stall region. Conversely, when the sail is experiencing a tailwind, and drag is to be maximised, we expect σ^* to place the angle of attack in the post-stall region, where the simple sinusoid captures this behaviour much better.

Figure 17 shows the optimal sail offset angle with respect to position for $V_r = 0$ and $V_r = 0.5$, both of which are regimes where the sail will experience both a tailwind and headwind at different points around the circular trajectory. We see in both cases that there are sections where the simple sinusoidal model closely matches the results using the experimental data, which corresponds to the drag-maximising, tailwind part of the sail's path. As expected, however, when the sail experiences a headwind (θ close to $0, 2\pi$), there is a much larger discrepancy with the simple model.

When the sail never experiences a tailwind ($V_r > 1$), we see a qualitative but not quantitative agreement between the models, since the angle of attack remains within the pre-stall region. This is shown in Figure 18. In this situation, where the sails are never expected to experience a high angle of attack, we may want to make a different simple approximation for the lift coefficient, only taking into account the pre-stall behaviour. The pre-stall region of the NACA-0012 airfoil lift coefficient is approximated well by $c_L \approx \sin 6\alpha$, which for small angles of attack approximately agrees with the classic thin airfoil result $c_L \approx 2\pi\alpha$ [44]. Using this alternative simple approximation for the lift coefficient, Figure 19 compares the resulting optimal sail offset angle with that obtained from the interpolated experimental data for $V_r = 1.5$. The close agreement between the two curves demonstrates that, when the sail operates entirely within the pre-stall regime, a simple approximation based solely on the small-angle lift characteristics is sufficient to reproduce the optimal sail orientation. We emphasise that we only changed the lift coefficient to approximate the pre-stall regime, and kept the drag coefficient the same, since the previous lift coefficient approximation was significantly less accurate at small angles of attack.

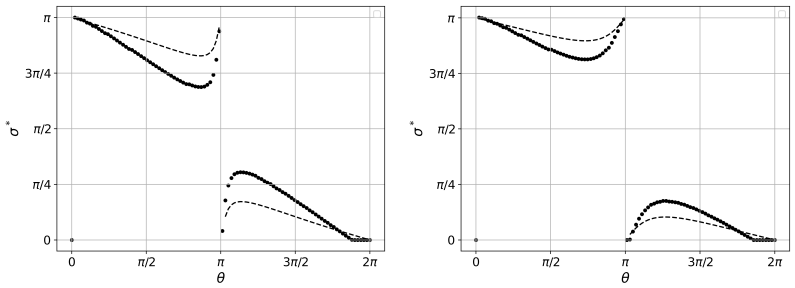


Fig. 18: The optimal sail offset angle σ^* vs position θ using the experimental lift and drag coefficients, with the simple sinusoidal model result shown as the dashed line. (Left) $V_r = 1.1$, (Right) $V_r = 1.5$.

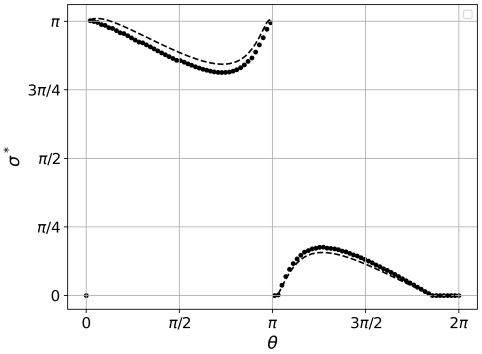


Fig. 19: The optimal sail offset angles σ^* for $V_r = 1.5$, using the experimental data interpolants (dotted) and a pre-stall approximation for the lift coefficient $c_L(\alpha) = \sin 6\alpha$ (dashed).

5 Physical Considerations and Limitations

The analysis presented has assumed an idealised mathematical framework to optimise sail-driven circular motion. However, real-world applications introduce several additional complexities that could influence both the accuracy of the model and the feasibility of implementation. This section outlines key physical considerations that must be addressed to bridge the gap between theoretical predictions and practical performance.

5.1 Sail Aerodynamics

The model assumes simple sinusoidal approximations for the lift and drag coefficients, but in reality, sail performance is highly dependent on aerodynamic factors. Curved sails, similar to asymmetric airfoils, generate lift more efficiently than flat plates, particularly at moderate angles of attack. At high angles of attack, flow separation

increases drag and reduces lift, leading to aerodynamic stall. Additionally, the aspect ratio of the sail influences vortex shedding and overall aerodynamic efficiency. Furthermore, rapid changes in sail orientation can induce transient flow phenomena that deviate from steady-state assumptions. In configurations with multiple sails, wake interactions become a significant factor, as downstream sails experience altered flow conditions due to turbulence generated by upstream sails. The brief investigation into using interpolants of experimental lift and drag coefficients takes into account some of these effects for a single sail, however, a more refined analysis should incorporate effects between sails.

5.2 Mechanical Constraints

The theoretical model assumes that sail orientation can be adjusted instantaneously; however, practical implementations are subject to mechanical limitations. Actuation systems introduce response delays, while high rotational speeds induce mechanical stresses that can restrict sail size and adjustability. Additionally, dynamic sail positioning requires active control mechanisms, which add complexity to the system's operation. These factors constrain the ability of the system to respond optimally to variations in wind speed and direction, reducing overall efficiency.

5.3 Wind Variability

The present model assumes a constant wind speed and direction, yet real-world wind conditions are highly variable. Fluctuations in wind speed and turbulence introduce additional challenges in maintaining optimal sail orientation. Rapid changes in wind direction may require continuous adjustments to sail angles, which could introduce inefficiencies if the response time of the adjustment mechanism is insufficient. Additionally, gusts can lead to sudden variations in aerodynamic forces, potentially affecting system stability. Future studies could consider incorporating stochastic wind models or real-time adaptive control strategies to account for these variations and improve robustness in dynamic environments.

5.4 Limitations of a Two-Dimensional Model

The current analysis is restricted to a two-dimensional framework, which simplifies the mathematical formulation but does not fully capture the three-dimensional nature of sail aerodynamics. In reality, sails experience complex three-dimensional flow patterns, including spanwise flow effects and induced drag, which are not accounted for in this model. Additionally, vertical wind shear and variations in aerodynamic forces across the height of a sail may significantly influence performance. Future extensions of this work could incorporate three-dimensional effects to improve applicability to real-world systems.

5.5 Implications for Future Research

To enhance the applicability of this model to real-world sail-driven energy systems, future research should focus on conducting CFD simulations to examine unsteady

aerodynamic effects between multiple sails, and developing control strategies for real-time sail adjustment. By including these considerations, the theoretical framework presented in this study can be further developed into a viable design tool for optimising sail-driven energy storage and propulsion systems.

6 Summary

This study developed a model to determine the optimal sail angle for generating torque in circular motion. By analysing the forces involved, including lift and drag under varying wind conditions and sail orientations, the model demonstrated that positive torque could be generated throughout most of the sail's circular path, except where headwind effects limit performance.

Key insights include the sensitivity of the optimal sail angle to the relative speeds of wind and sail. When the sail speed is lower than the wind speed, the sail encounters favourable tailwind effects on part of its path, allowing for higher torque generation due to drag. Conversely, when the sail speed exceeds the wind speed, the sail continuously faces partial headwinds, making it more advantageous to minimise drag by aligning the sail more closely with the apparent wind direction, and using lift forces to generate advantageous torque. These findings underscore the importance of managing sail angles dynamically to maximise power generation.

The analysis was extended to multiple sails, revealing that increasing the number of sails reduces torque variance over a rotation cycle. This suggests that in practical applications, with a sufficient number of sails, torque output would remain almost steady, promoting stable energy generation for a given wind speed and rotational velocity. However, as the system's rotational velocity increases, the sails begin to counteract the device's rotation due to headwind forces, highlighting a rotational speed threshold beyond which the sails may hinder rather than aid the system's performance.

Further research should focus on accurately determining the lift and drag coefficients for the specific sails to be used in practice, as the model's predictions are highly sensitive to these factors. Additionally, engineering considerations should evaluate the benefits of positioning the sails at varying radii, as the optimal placement may shift depending on operational speeds and system constraints. Practical implementation will also require assessing and mitigating potential interference between multiple sails and addressing the effects of downwind forces on the overall structure.

In conclusion, this study provides a foundational model for sail-driven torque optimisation in rotating wind systems. With targeted adjustments, *Gyrerg* and similar systems could leverage these insights to enhance their wind energy capture capabilities, potentially contributing to more sustainable and efficient energy storage solutions.

Acknowledgements. We would like to thank Peter Roberts, Robert Kettle and Lars Boerner from VerdErg Renewable Energy Limited for financial support for this project, and for many helpful discussions over the course of this research.

Declarations

- Funding: Rory Ward received payment from VerdErg Renewable Energy Ltd for work undertaken as part of an industry project during their Master's degree, on which this study is based.
- Conflict of interest/Competing interests: Rory Ward reports financial support was provided by VerdErg Renewable Energy Ltd. The other authors declare that they have no known competing financial interests or personal relationships that could have appeared to influence the work reported in this paper.
- Ethics approval and consent to participate: Not applicable
- Consent for publication: Not applicable
- Data availability: No new data was produced in this research. The lift and drag coefficient data used in Figures 5 and 16 were taken from https://doi.org/10.2172/6548367.
- Materials availability: Not applicable
- Code availability: All code used to produce the figures is available in this GitHub repository: https://github.com/RCWard01/OptimalSailAnglesToDriveCircularMotion.git
- Author contribution - CRediT Taxonomy:
  Conceptualisation: Rory Ward, Ian Hewitt; Formal Analysis: Rory Ward; Investigation: Rory Ward; Methodology: Rory Ward, Ian Hewitt, Graham Benham; Project Administration: Ian Hewitt; Resources: Rory Ward; Software: Rory Ward; Supervision: Ian Hewitt, Graham Benham; Validation: Rory Ward, Ian Hewitt, Graham Benham; Visualisation: Rory Ward; Writing - original draft: Rory Ward; Writing - review and editing: Rory Ward, Ian Hewitt, Graham Benham

References

[1] Suberu, M.Y., Mustafa, M.W., Bashir, N.: Energy storage systems for renewable energy power sector integration and mitigation of intermittency. Renewable and Sustainable Energy Reviews **35**, 499–514 (2014) https://doi.org/10.1016/j.rser.2014.04.009

[2] Department for Energy Security and Net Zero: Net Zero Government Initiative. Technical report, Department for Energy Security and Net Zero (December 2023)

[3] Fares, R.: Renewable Energy Intermittency Explained: Challenges, Solutions, and Opportunities — scientificamerican.com. https://www.scientificamerican.com/blog/plugged-in/renewable-energy-intermittency-explained-challenges-solutions-and-opportunities/. Accessed: 18-08-2024 (2015)

[4] Dehghani-Sanij, A.R., Tharumalingam, E., Dusseault, M.B., Fraser, R.: Study of energy storage systems and environmental challenges of batteries. Renewable and Sustainable Energy Reviews **104**, 192–208 (2019) https://doi.org/10.1016/j.rser.2019.01.023

[5] Baines, J.A., Newman, V.G., Hanna, I.W., Douglas, T.H., Carlyle, W.J., Jones, I.L., Eaton, D.M., Zeronian, G.: Dinorwig Pumped Storage Scheme. Part 1: Design. Part 2: Construction. Proceedings of the Institution of Civil Engineers **74**(4), 637–718 (1983) https://doi.org/10.1680/iicep.1983.1360

[6] Kim, S.W., Park, S.G., Lee, E.J.: Assessment of the explosion risk during lithium-ion battery fires. Journal of Loss Prevention in the Process Industries **80**, 104851 (2022) https://doi.org/10.1016/j.jlp.2022.104851

[7] Yang, Y., Bremner, S., Menictas, C., Kay, M.: Modelling and optimal energy management for battery energy storage systems in renewable energy systems: A review. Renewable and Sustainable Energy Reviews **167**, 112671 (2022) https://doi.org/10.1016/j.rser.2022.112671

[8] Sim, S.B., Lee, C.H., Kim, S.K.: Study on the explosion and fire risks of lithium batteries due to high temperature and short circuit current. Fire Science and Engineering **30**(2), 114–122 (2016) https://doi.org/10.7731/kifse.2016.30.2.114

[9] Costa, C.M., Barbosa, J.C., Goncalyes, R., Castro, H., Del Campo, F.J., Lanceros-Méndez, S.: Recycling and environmental issues of lithium-ion batteries: Advances, challenges and opportunities. Energy Storage Materials **37**, 433–465 (2021) https://doi.org/10.1016/j.ensm.2021.02.032

[10] Alva, G., Lin, Y., Fang, G.: An overview of thermal energy storage systems. Energy **144**, 341–378 (2018) https://doi.org/10.1016/j.energy.2017.12.037

[11] Sarbu, I., Sebarchievici, C.: A comprehensive review of thermal energy storage. Sustainability **10**(1), 191 (2018) https://doi.org/10.3390/su10010191

[12] Andersson, J., Grönkvist, S.: Large-scale storage of hydrogen. International Journal of Hydrogen Energy **44**(23), 11901–11919 (2019) https://doi.org/10.1016/j.ijhydene.2019.03.063

[13] Budt, M., Wolf, D., Span, R., Yan, J.: A review on compressed air energy storage: Basic principles, past milestones and recent developments. Applied Energy **170**, 250–268 (2016) https://doi.org/10.1016/j.apenergy.2016.02.108

[14] VerdErg Renewable Energy: Gyrerg: Wind Energy Storage on a Gigawatt-Scale. https://www.verderg.com/gyrerg. Accessed: 12-08-2024 (2022)

[15] VerdErg Renewable Energy: About Us. https://www.verderg.com/about-us. Accessed: 12-08-2024 (2022)

[16] Thwaite, B.: The aerodynamic theory of sails. i. two-dimensional sails. Proceedings of the Royal Society of London. Series A. Mathematical and Physical Sciences **261**(1306), 402–422 (1961) https://doi.org/10.1098/rspa.1961.0086

[17] Newman, B.G.: Aerodynamic theory for membranes and sails. Progress in Aerospace Sciences **24**(1), 1–27 (1987) https://doi.org/10.1016/0376-0421(87)90005-4

[18] Saoud, H., Hua, M.-D., Plumet, F., Ben Amar, F.: Optimal sail angle computation for an autonomous sailboat robot. In: 2015 54th IEEE Conference on Decision and Control (CDC), pp. 807–813 (2015). https://doi.org/10.1109/CDC.2015.7402329

[19] Viola, I.M., Flay, R.G.J.: Sail aerodynamics: Understanding pressure distributions on upwind sails. Experimental Thermal and Fluid Science **35**(8), 1497–1504 (2011) https://doi.org/10.1016/j.expthermflusci.2011.06.009

[20] Fossati, F., Muggiasca, S.: Experimental investigation of sail aerodynamic behavior in dynamic conditions. Journal of Sailing Technology **2**(8), 1–41 (2011)

[21] Kjellberg, M., Gerhardt, F., Werner, S.: Sailing performance of wind-powered cargo vessel in unsteady conditions. Journal of Sailing Technology **8**(01), 218–254 (2023) https://doi.org/10.5957/jst/2023.8.12.218

[22] Angelou, M., Spyrou, K.J.: Dynamic stability assessment of yacht downwind sailing in regular waves. Applied Ocean Research **111**, 102651 (2021) https://doi.org/10.1016/j.apor.2021.102651

[23] Abhinaya, V., Kumar, G.G.: A comprehensive review on h-type darrieus wind turbine: aerodynamics, blade profile, cfd simulations. Journal of Engineering and Applied Science **73**(1) (2026) https://doi.org/10.1186/s44147-026-00968-x

[24] Kirke, B.K., Paillard, B.: Predicted and measured performance of a vertical axis wind turbine with passive variable pitch compared to fixed pitch. Wind Engineering **41**(1), 74–90 (2016) https://doi.org/10.1177/0309524x16677884

[25] Bianchini, A., Ferrara, G., Ferrari, L.: Pitch optimization in small-size darrieus wind turbines. Energy Procedia **81**, 122–132 (2015) https://doi.org/10.1016/j.egypro.2015.12.067

[26] Rezaeiha, A., Kalkman, I., Blocken, B.: Effect of pitch angle on power performance and aerodynamics of a vertical axis wind turbine. Applied Energy **197**, 132–150 (2017) https://doi.org/10.1016/j.apenergy.2017.03.128

[27] Elkhoury, M., Kiwata, T., Aoun, E.: Experimental and numerical investigation of a three-dimensional vertical-axis wind turbine with variable-pitch. Journal of Wind Engineering and Industrial Aerodynamics **139**, 111–123 (2015) https://doi.org/10.1016/j.jweia.2015.01.004

[28] Li, C., Xiao, Y., Xu, Y.-l., Peng, Y.-x., Hu, G., Zhu, S.: Optimization of blade pitch in h-rotor vertical axis wind turbines through computational fluid dynamics simulations. Applied Energy **212**, 1107–1125 (2018) https://doi.org/10.1016/j.

apenergy.2017.12.035

[29] Gupta, A., Abderrahmane, H.A., Janajreh, I.: Flow analysis and sensitivity study of vertical-axis wind turbine under variable pitching. Applied Energy **358**, 122648 (2024) https://doi.org/10.1016/j.apenergy.2024.122648

[30] Abdalrahman, G., Melek, W., Lien, F.-S.: Pitch angle control for a small-scale darrieus vertical axis wind turbine with straight blades (h-type vawt). Renewable Energy **114**, 1353–1362 (2017) https://doi.org/10.1016/j.renene.2017.07.068

[31] Abbaszadeh, S., Hoerner, S., Maître, T., Leidhold, R.: Experimental investigation of an optimised pitch control for a vertical-axis turbine. IET Renewable Power Generation **13**(16), 3106–3112 (2019) https://doi.org/10.1049/iet-rpg.2019.0309

[32] Horb, S., Fuchs, R., Immas, A., Silvert, F., Deglaire, P.: Variable pitch control for vertical-axis wind turbines. Wind Engineering **42**(2), 128–135 (2018) https://doi.org/10.1177/0309524x18756972

[33] Ma, K., Wang, J., Lin, K.: A novel variable pitch control strategy to improve the aerodynamics of vertical axis wind turbine. Physics of Fluids **37**(3) (2025) https://doi.org/10.1063/5.0254998

[34] Delafin, P.-L., Deniset, F., Astolfi, J.A., Hauville, F.: Performance improvement of a darrieus tidal turbine with active variable pitch. Energies **14**(3), 667 (2021) https://doi.org/10.3390/en14030667

[35] Sheldahl, R.E., Klimas, P.C.: Aerodynamic characteristics of seven symmetrical airfoil sections through 180-degree angle of attack for use in aerodynamic analysis of vertical axis wind turbines. Technical report, Office of Scientific and Technical Information (OSTI) (March 1981). https://doi.org/10.2172/6548367 . http://dx.doi.org/10.2172/6548367

[36] Nafroni, N., W., R.B., Adripta, P.: Effect of Variation of Angle of Attack on Lift and Drag Coefficient of Flat Plate Wing on Flying Inflatable Boat. In: Proceedings of the International Conference on Sustainable Engineering, Infrastructure and Development, ICO-SEID 2022, 23-24 November 2022, Jakarta, Indonesia. EAI, ??? (2023). https://doi.org/10.4108/eai.23-11-2022.2341594

[37] Sogukpinar, H., Bozkurt, I.: Calculation of aerodynamic performance characteristics of airplane wing and comparing with the experimental measurement. International Journal of Engineering Technologies, IJET **1**(2), 83 (2015) https://doi.org/10.19072/ijet.87923

[38] Fearn, R.L.: Potential Flow over a NACA Four-Digit Airfoil. Wolfram Demonstrations Project (2008). https://demonstrations.wolfram.com/PotentialFlowOverANACAFourDigitAirfoil/

[39] Anderson, B.D.: The physics of sailing. Physics Today **61**(2), 38–43 (2008) https://doi.org/10.1063/1.2883908

[40] Gentry, A.: The aerodynamics of sail interaction. In: Proceedings of the Third AIAA Symposium on the Aero/Hydronautics of Sailing (1971)

[41] Richards, P.J., Le Pelley, D.J., Jowett, D., Little, J., Detlefsen, O.: A wind tunnel study of the interaction between two sailing yachts. In: Day 2 Sat, March 16, 2013. CSYS13. SNAME, ??? (2013). https://doi.org/10.5957/csys-2013-012 . http://dx.doi.org/10.5957/CSYS-2013-012

[42] Meyers, J., Meneveau, C.: Optimal turbine spacing in fully developed wind farm boundary layers. Wind Energy **15**(2), 305–317 (2011) https://doi.org/10.1002/we.469

[43] Newman, B.G.: The spacing of wind turbines in large arrays. Energy Conversion **16**(4), 169–171 (1977) https://doi.org/10.1016/0013-7480(77)90024-9

[44] Anderson, J.D.: Fundamentals of Aerodynamics, 5th edn., p. 344. McGraw-Hill, ??? (2011). http://www.worldcat.org/isbn/9780073398105